Advanced Materials

ADVANCED MATERIALS
www.advmat.de

RESEARCH ARTICLE

Charge Carrier and Spin Transport Properties in Diketopyrrolopyrrole-Based Polymers

Xitong Liu[1,2] | Congyuan Wei[1] | Hao Li[1,2] | Zhen Yang[3] | Youjia Li[4] | Mengya Liu[1] | Zhihui Chen[1] | Weifeng Zhang[1,2] | Liping Wang[4] | Kuijuan Jin[3,5] | Gui Yu[1,2]

[1]Beijing National Laboratory For Molecular Sciences, CAS Research/Education Center For Excellence in Molecular Sciences, Institute of Chemistry, Chinese Academy of Sciences, Beijing, P. R. China | [2]School of Chemical Sciences, University of Chinese Academy of Sciences, Beijing, P. R. China | [3]Beijing National Laboratory For Condensed Matter Physics, Institute of Physics, Chinese Academy of Sciences, Beijing, P. R. China | [4]School of Materials Science and Engineering, University of Science and Technology Beijing, Beijing, P. R. China | [5]School of Physical Sciences, University of Chinese Academy of Sciences, Beijing, P. R. China

Correspondence: Liping Wang (lpwang@mater.ustb.edu.cn) | Kuijuan Jin (kjjin@iphy.ac.cn) | Gui Yu (yugui@iccas.ac.cn)

Received: 20 July 2025 | **Revised:** 22 November 2025 | **Accepted:** 28 January 2026

Keywords: D–A copolymers | electron mobilities | magnetoresistance | organic spin-valves | spin transport

ABSTRACT

The organic active layer in organic spin-valves (OSVs) plays a vital role in regulating the device's performance, and the variations in molecular structure can significantly modulate their physicochemical properties. Herein, we synthesized two diketopyrrolopyrrole-based donor-acceptor copolymers with distinct alkyl side chains, namely DPP-BTCN-C1 (with side-chain branching points closer to the conjugated skeleton) and DPP-BTCN-C3. To evaluate the charge carrier transport properties, a polymer field-effect transistor and space charge limited current method based on the two molecules were conducted. The experimental results demonstrated that the DPP-BTCN-C1 materials had a higher electron transport mobility. Moreover, the spin transport properties were also revealed by fabricating OSVs devices. In the OSVs with a 50 nm interlayer, DPP-BTCN-C1 exhibited a higher magnetoresistance (RM) value of up to 24.6 %. By fitting the polymer thickness dependence of the MR value at 10 K, a longer spin diffusion length and higher spin polarization injection efficiency were achieved for the DPP-BTCN-C1 structure. We attributed the differences in charge and spin transport performance to the modulation of the film microstructure and energy levels by the alkyl side chains. This work studied the structure-property relationship of polymer OSVs from the perspective of side-chain engineering, providing valuable insights for the design of polymers with enhanced spin properties.

1 | Introduction

With the rapid advancement of information technology, spintronics, which utilizes the electron spin degree of freedom for data storage and logical operations, has garnered significant attention in the academic community [1–3]. In the meanwhile, organic semiconductors (OSCs), which are typically composed of lightweight elements including carbon, hydrogen and oxygen, exhibit intrinsic weak spin orbit coupling and hyperfine interaction [4–6]. Thus, the integration of OSCs with exceptional spin transport potential into spintronics has led to the emergence of a new interdisciplinary field: organic spintronics [7, 8]. Since the initial fabrication of organic spin-valves (OSVs) by Xiong et al. [9], organic spintronics has witnessed numerous advancements over the past two decades of intensive research. A variety of material types and spinterface modification methods have been

Xitong Liu, Congyuan Wei, and Hao Li contributed equally to this work.

applied in this field. In addition, organic spintronic functional devices have also been developed and optimized. In the realm of material development, alongside small molecules and polymers [10, 11], several novel material systems, including metal organic frameworks [12, 13], covalent organic frameworks [14], radicals [15, 16], and organic–inorganic hybrid perovskites [17, 18], have also been employed as spin transport layers. In recent years, certain polymers exhibiting unique physical properties, such as ferromagnetic [19] or ferroelectric characteristics [20, 21], have been increasingly employed in the field of organic spintronics, thereby significantly broadening the range of physical phenomena and control strategies associated with spin valve devices. Moreover, the deeper investigation into the impact of OSCs' structure on spin-related properties is crucial for the design of intrinsically high-performance materials. As a crucial component of OSCs, π-conjugated polymers have been extensively investigated and utilized in various organic electronic devices, including organic field-effect transistors and organic photovoltaic devices [22, 23]. The intrinsic flexibility, stretchability, and compatibility with solution processing of polymer materials also render them highly attractive for research in the field of organic spintronics [24, 25]. The research on conjugated polymers in spintronics devices primarily focused on the following aspects: (1) investigating the structure-properties correlations by leveraging the structural diversity [26, 27]; (2) enhancing spin transport properties through tailored chemical structures or doping strategies [28, 29]; (3) providing a material foundation for the development of functional devices [30, 31].

On the other hand, Li et al. were the first to attempt the fabrication of OSVs devices based on donor-acceptor (D–A) copolymers, achieving excellent spin transport performance [32]. The D–A strategy adopted by polymers facilitated intermolecular π–π stacking, enabling more effective regulation of energy level and enhanced material stability [33, 34]. Consequently, the D–A type polymer has also attracted attention for its application in organic spintronics. For instance, Li et al. investigated the effect of the introduction of the pyridine nitrogen atom and the substitution of the fluorine atom in the isoindigo acceptor unit on the spin transport properties of the resulting polymers [35]. Zheng et al. achieved room-temperature spin transport abilities in ambipolar naphthalenediimide-based conjugated polymers [36]. Moreover, the magnetoresistance (MR) response and spinterface effect based on diketopyrrolopyrrole (DPP) building blocks were discovered by Zheng et al. [37]. More recently, Yang et al. examined the impact of halogen substitution on the spin relaxation of bay-annulated indigo-based D–A polymers [38]. Nevertheless, research on the spintronic properties of D–A polymers remains in its nascent stages and is not as well-developed as the studies on charge transport properties in polymer field-effect transistors (PFETs) [39, 40]. Consequently, the full potential of these materials in the field of spintronics has yet to be fully realized. Investigating the effect of molecular structure modification on the physicochemical properties of materials, and consequently on the modulation of their spin transport performance, is of significant importance.

In this study, two DPP-based D–A polymers with different side-chain branching points were synthesized, in which the alkyl chain branching point of DPP-BTCN-C3 is further away from the conjugated skeletons than that of DPP-BTCN-C1. Initially, to evaluate the transport characteristics of charge carriers, the carrier mobilities of the polymer films in the horizontal and vertical directions were measured by using PFET devices and the space charge limited current (SCLC) method, respectively. Compared with DPP-BTCN-C3, DPP-BTCN-C1 material exhibited higher electron mobility in both the horizontal and vertical directions. Ultimately, OSVs devices based on these two polymers were fabricated in order to investigate the spin-polarized carriers transport properties. Under identical OSVs fabrication conditions, devices based on DPP-BTCN-C1 presented an obviously larger MR value compared to those based on DPP-BTCN-C3. By fitting the correlation between the MR value and the thickness of the transport layer, we observed a higher spin diffusion length and spin polarization injection efficiency in DPP-BTCN-C1 polymer at 10 K. Through further characterization, we found that the introduction of different alkyl side chains modulated the microstructure and molecular orbital energy levels of the D–A polymers, consequently affecting its charge and spin transport properties. Our work attempts to explore the influence of the side-chain on spin transport properties in D–A polymers, with the goal of promoting the development of such materials in the field of organic spintronics.

2 | Results and Discussion

The DPP unit served as a critical acceptor component in D–A polymer semiconductor materials, playing a pivotal role in the development of high-mobility polymers in PFETs. Given that high mobility is considered advantageous for long spin relaxation length, DPP-based polymers have also been favored in spintronics. As illustrated in Scheme 1, we polymerized the DPP unit with the [2,2′-bithiophene]-3,3′-dicarbonitrile (BTCN) building blocks via Stille coupling and modified the resulting polymers with varying alkyl chains. The distinct alkyl side chains of the DPP-BTCN-C1 and DPP-BTCN-C3 polymers were 2-decyltetradecyl (C1) and 4-decyltetradecyl (C3), respectively.

The chemical structures of the two polymers were measured by using high-temperature ^{1}H NMR as shown in Figure S1. In addition, the thermal property analyses of the polymers were carried out by using thermalgravimetric analysis and differential scanning calorimetry. The decomposition temperature (T_d, 5 % loss of polymeric weight) was determined to be 433°C for DPP-BTCN-C1, while DPP-BTCN-C3 proved a higher T_d of 451°C (Figure S2). In addition, no obvious exothermic and endothermic transitions were found in the two polymers, indicating no obvious phase transitions in the range of 50°C–250°C (Figure S3). The experimental results confirmed that both polymers exhibited excellent thermal stability.

As shown in Figure 1, the optical properties of the two copolymers were studied by using UV–vis–NIR absorption spectra. The absorption characteristics of the two polymers were investigated in both diluted chloroform solution and thin film states. Both polymers demonstrated dual-band absorption profiles from 350 to 1000 nm. The broad low-energy absorption bands observed in the 520–1000 nm can be assigned to intermolecular charge transfer, which arose from the strong electron "push-pull" interaction between DPP and BTCN units [41]. Moreover, polymer

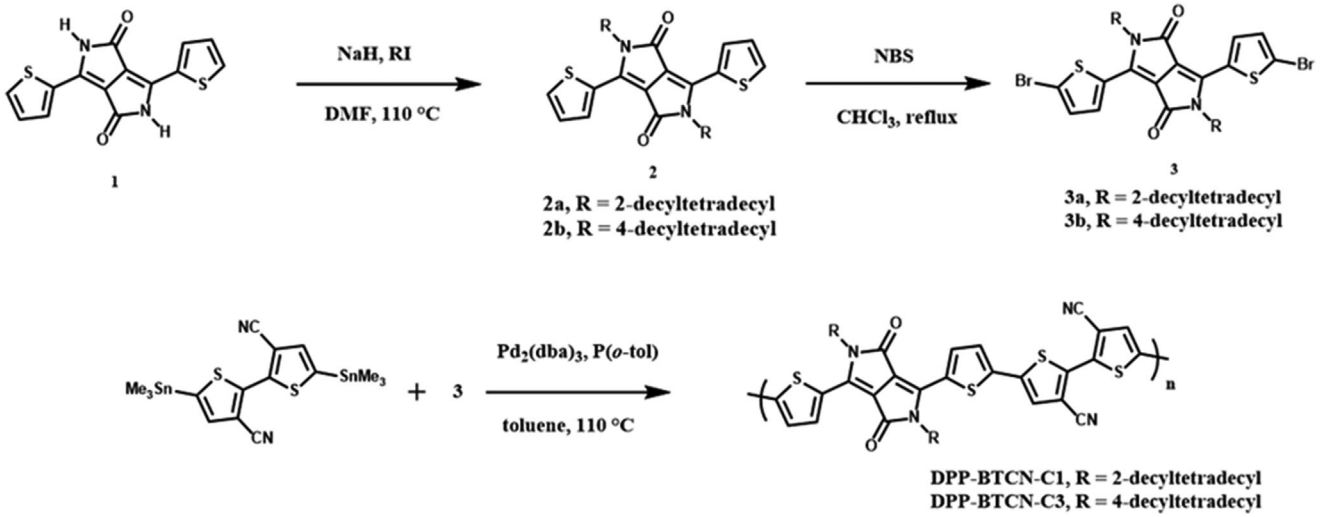

SCHEME 1 | The molecular structures and synthesis routes of the conjugated polymer.

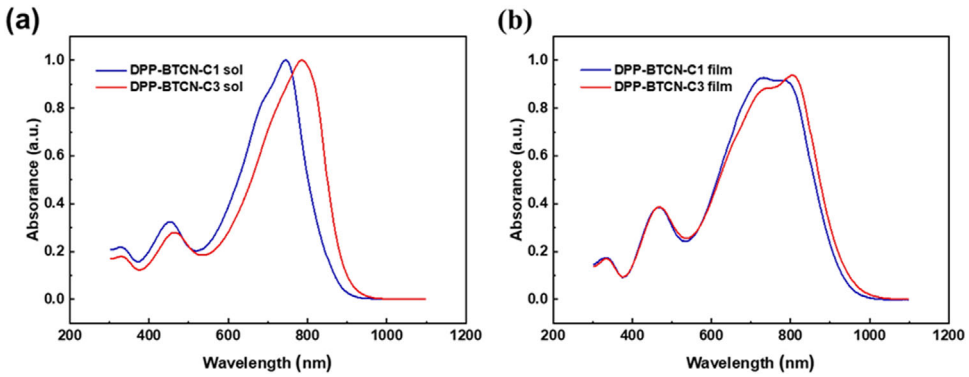

FIGURE 1 | UV–vis–NIR absorption spectra of DPP-BTCN-C1 and DPP-BTCN-C3 copolymers in dilute chloroform solutions (a) and thin films prepared in quartz plates (b).

DPP-BTCN-C1 proved a slightly blueshifted absorption, presumably due to the introduction of different alkyl side chains. In addition, the absorption in the thin film state exhibited a broader profile compared to that in the solution state. In comparison with the λabs max of 802 nm in the DPP-BTCN-C3 thin film state, the DPP-BTCN-C1-based film presented a higher intensity of the 0–1 vibrational peak (with λabs max of 732 nm) than that of the 0–0 vibration peak. An H-type dominated aggregation would be preferred during the solution-to-solid planarization process. The optical band (Eopt g) calculated from the thin-film absorption edge (λabs edge) was 1.34 and 1.31 eV for DPP-BTCN-C1 and DPP-BTCN-C3, respectively.

To investigate the electrochemical properties of the polymers, cyclic voltammetry (CV) and ultraviolet photoelectron spectroscopy (UPS) measurements were conducted to measure the frontier molecular orbital energy levels of both copolymers. CV analyses of the two polymers were performed under an Ar atmosphere to determine their electrochemical properties. Polymer solutions in chloroform were deposited onto the surface of a glassy carbon electrode to ensure uniform films on the working electrode. The working electrode was immersed in the electrolyte solution (0.1 M tetrabutylammonium hexafluorophosphate in anhydrous acetonitrile), along with an Ag/AgCl reference electrode (0.1 M KCl) and a Pt wire counter electrode. Ferrocene$^+$/ferrocene, as an external calibration, was utilized to validate the CV measurements [42]. As presented in Figure S4, both polymers showed obvious oxidation and reduction processes. The onset potentials of the oxidation and reduction peaks determined energy levels of their highest occupied molecular orbital (HOMO) and lowest unoccupied molecular orbital (LUMO). The HOMO and LUMO energy levels for DPP-BTCN-C1 and DPP-BTCN-C3 were −5.63/−3.56 and −5.56/−3.53 eV, respectively. To further corroborate the HOMO energy levels of the polymer, UPS analyses were performed on the spin-coated thin films on ITO substrates under He-I discharge at 21.22 eV. As shown in Figure 2, the secondary electron cutoffs (E_{cutoff}) and onset of HOMO ($E_{\text{H,onset}}$) for DPP-BTCN-C1 and DPP-BTCN-C3 were measured to be 16.63/1.13 eV and 16.88/1.26 eV, respectively. According to the ionization potentials (IP) equation, IP = $h\nu$–(E_{cutoff} − $E_{\text{H,onset}}$) (1), the EUPS HOMO were calculated to be −5.72 and −5.60 eV for DPP-BTCN-C1 and DPP-BTCN-C3, respectively. Combined with the results of the optical bandgaps, we determined the HOMO/LUMO energy levels of the DPP-BTCN-C1 and DPP-BTCN-C3 to be −5.72/−4.38 eV and −5.60/−4.29 eV, respectively (Table 1). In the solid-state thin

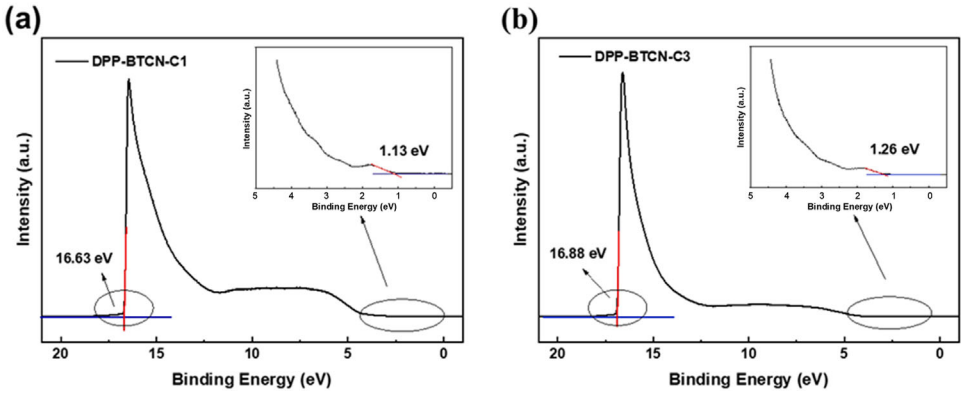

FIGURE 2 | UPS measurements for (a) DPP-BTCN-C1 and (b) DPP-BTCN-C3 thin films with $h\nu = 21.22$ eV.

TABLE 1 | Optical and Electrochemical Properties of the Two Polymers.

Polymers	E_g^{opt} (eV)	E_{HOMO}^{CV} (eV)	E_{LUMO}^{CV} (eV)	IP[a] (eV)	EA[b] (eV)
DPP-BTCN-C1	1.34	−5.63	−3.56	5.72	4.38
DPP-BTCN-C3	1.31	−5.56	−3.53	5.60	4.29

[a]IP measured by the UPS.

[b]EA representing electron affinity determined by calculations involving optical bandgaps and IPs.

film measurements, the frontier orbit energy levels evaluated by using UPS are more reliable compared to those obtained from CV analyses.

In accordance with the spin diffusion length formula, $\lambda_s = \sqrt{\mu k_B T \tau / e}$ (2), the transport capability of charge carriers significantly influenced the efficiency of spin transport within the thermally activated hopping mechanism [32, 43]. Therefore, charge-carrier transport properties of the two copolymers in both the horizontal and vertical directions were systematically investigated. First, to investigate the charge transport properties of the polymer in the horizontal direction, PFET devices with a top-gate/bottom-contact (TGBC) configuration were fabricated on Coning glass, in which the encapsulation effect of the top gate electrodes ensured the stability for electron transport. The fabrication process of the devices was introduced in detail in the Experimental Section. The transfer and output curves were represented in Figure 3 and Figure S5. All the polymers demonstrated ambipolar charge transport behaviors, with a pronounced electron-dominated mobility accompanying weak hole transport. As summarized in Table 2, the DPP-BTCN-C1-based PFETs demonstrated a maximum electron mobility ($\mu_{e,\,max}$) of 0.36 $cm^2\ V^{-1}\ s^{-1}$ and a maximum hole mobility ($\mu_{h,\,max}$) of 3.9×10^{-3} $cm^2\ V^{-1}\ s^{-1}$. Meanwhile, a lower $\mu_{e,\,max}$ of 0.24 $cm^2\ V^{-1}\ s^{-1}$ and a slightly higher $\mu_{h,\,max}$ of 7.5×10^{-3} $cm^2\ V^{-1}\ s^{-1}$ were calculated in DPP-BTCN-C3-based PFETs. Moreover, the charge mobility measurements of the polymer thin films in the vertical direction were obtained by using SCLC methods [44, 45]. As shown in Figure S6, the calculated electron mobilities in the vertical direction for the annealed DPP-BTCN-C1 and DPP-BTCN-C3 films were 3.52×10^{-5} and 2.59×10^{-5} $cm^2\ V^{-1}\ s^{-1}$, respectively (details were discussed in the Supporting Information).

Therefore, we surmised that the lower LUMO energy level was one of the primary factors contributing to the enhanced electron mobility in DPP-BTCN-C1 polymer thin films.

To explore the spin transport properties, OSVs devices based on the two polymers were fabricated. OSVs with a stacking architecture of $La_{0.67}Sr_{0.33}MnO_3$ (LSMO)/D–A polymers/Co/Au were prepared with a junction area of $200 \times 200\ \mu m^2$ (Figure 4a). The ferromagnetic (FM) LSMO and Co electrodes worked as the spin injectors and detectors, respectively, and the polymer layers acted as a spin transport interlayer. By employing FM electrodes with varying coercive fields, the OSVs device exhibited distinct magnetization configurations under different magnetic fields, thereby influencing the transport of spin-polarized carriers. We used MR values to evaluate the performance of the OSVs devices, in which the MR value was typically defined by the equation, $MR = (R_{ap}\text{-}R_p)/R_p$ (3), where R_{ap} and R_p represented the resistance in antiparallel and parallel device configurations, respectively. The half-metallic LSMO electrode was commonly utilized in the fabrication of OSVs devices owing to its high spin polarization efficiency at low temperature and excellent ambient stability. To compare the spin transport properties of the two polymers, spin-valve devices were measured in a physical property measurement system (PPMS) by a pseudo-four-probe method. As shown in Figure 4b,c, the MR curves obtained for both polymers with an interlayer thickness of 70 nm exhibited a pronounced positive MR effect. The polymeric spin-valves based on DPP-BTCN-C1 could achieve a positive MR valve of around 20 % at 10 K, and the magnitude of the MR signal exhibited a sharp decline with increasing temperature, which is attributed to the reduction in spin polarization of the LSMO electrode. In addition, we observed that the MR signal value of the spin-valve devices based on DPP-BTCN-C3 was slightly lower than that of the device based on DPP-BTCN-C1 (Figure 4d). This result indicated a superior

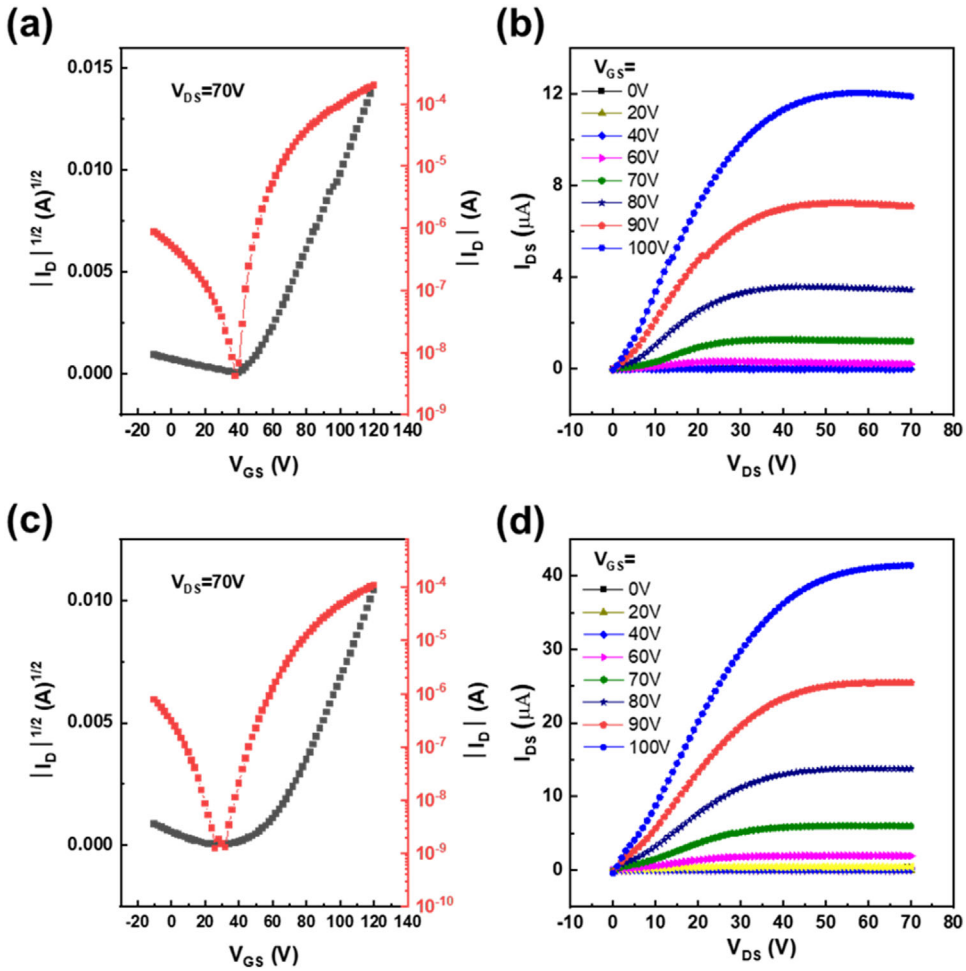

FIGURE 3 | Transfer and output characteristic curves for measuring electron mobility. (a,b) Typical (a) transfer and (b) output characteristics of the DPP-BTCN-C1-based PFETs. (c,d) Typical (c) transfer and (d) output characteristics of the DPP-BTCN-C3-based PFETs.

TABLE 2 | Device performance of PFETs based on the two polymers.

Polymers	*n-channel*				*p-channel*			
	$\mu_{max(cm^2\,V^{-1}\,s^{-1})}$	$\mu_{ave(cm^2\,V^{-1}\,s^{-1})}$	V_{th} (V)	I_{on}/I_{off}	$\mu_{max(cm^2\,V^{-1}\,s^{-1})}$	$\mu_{ave(cm^2\,V^{-1}\,s^{-1})}$	V_{th} (V)	I_{on}/I_{off}
DPP-BTCN-C1	0.36	0.26	45 ± 5	10^4–10^5	3.9×10^{-3}	2.97×10^{-3}	38 ± 5	10^2–10^3
DPP-BTCN-C3	0.24	0.17	55 ± 5	10^4–10^5	7.5×10^{-3}	5.8×10^{-3}	55 ± 5	10^3–10^4

Mobility is calculated based on the results from more than 10 devices

spin transport performance in the DPP-BTCN-C1 materials. To validate the origin of the MR responses, we characterized the magnetic hysteresis loops of the FM electrodes via a vibrating sample magnetometer (VSM). As shown in Figure 5a,b, the M-H traces of the Co electrode thermal-deposited on the polymer thin film and the LSMO electrode demonstrated different coercivity behaviors. Thus, the difference in coercive switching points was assigned to the origin of the MR effect. Moreover, we found that the coercive fields of the Co electrodes deposited on the DPP-BTCN-C1 and DPP-BTCN-C3 films also exhibited a slight difference, which could be attributed to the interface hybridization between the FM electrodes and the polymer materials. In the meantime, electrical measurements were conducted to obtain the spin-polarized carriers transport mechanism of the polymeric spin-valves. The *I–V* characteristic of both devices displayed pronounced nonlinearity at various temperatures, proving compelling evidence of non-ohmic contact between the FM electrodes and the polymer interlayer (Figure 5c,d). What's more, the *I–V* curves exhibited a monotonous temperature-dependent relationship, that is, the resistance of the OSVs devices decreased with increasing temperature. The above results indicated that in the OSVs devices, effective carrier injection was achieved and the hopping transport mechanism was adopted, with no interference from metallic filaments or magnetic inclusions.

To further investigate the impact of the distance from the side-chain branching points to the main chain on spin injection and

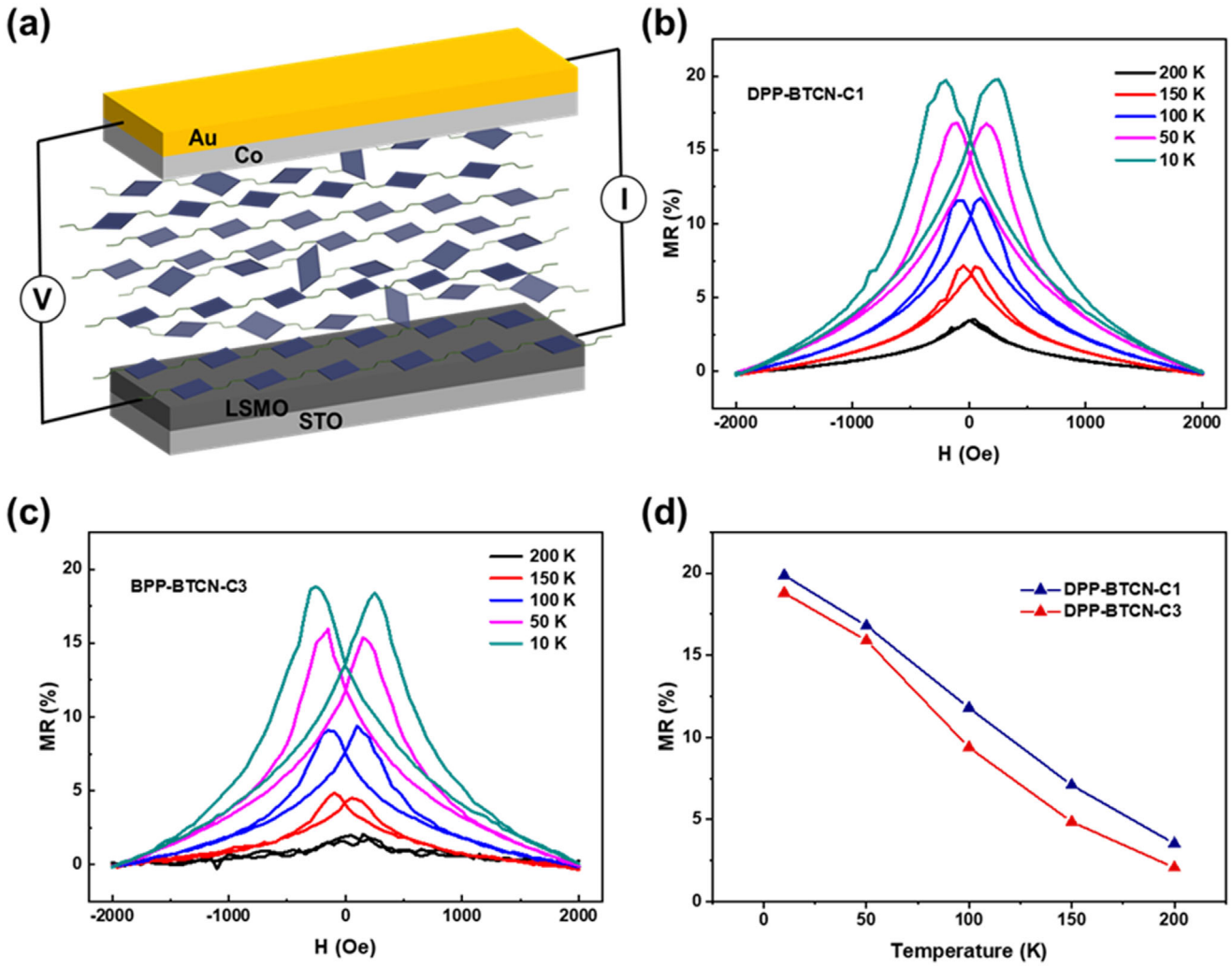

FIGURE 4 | The properties of OSVs. (a) Device structure of polymer OSVs with a stacking architecture of $SrTiO_3$/LSMO/polymer/Co/Au. (b,c) The MR curves of (b) DPP-BTCN-C1 and (c) DPP-BTCN-C3 based devices at 0.1 μA are measured at different temperatures. (d) The summary of the MR ratios of the devices varies with temperature.

spin transport properties, we systematically varied the thickness of the polymer layer to establish its correlation with the magnitude of the MR value. By adjusting the solution concentration and the spin-casting speed, we controlled the thickness of the polymer films to approximately 50, 70, 100, and 140 nm, and the corresponding MR signals were successfully acquired (Figure 6a; Figure S7). If the thickness of the polymer film is excessively thin, it may lead to the formation of a tunneling region. Conversely, the spin transport cannot effectively traverse the excessively thick polymer films, resulting in an inability to detect the MR signal. The modified Julliere formula was applied to extract the spin diffusion lengths of the two polymers. Taking into account the decay of the spin polarization of the carriers during the transport in the OSCs layer, the MR ratio can be expressed as follows:

$$MR = \frac{2p_1p_2e^{-(d-d_0)/\lambda_s}}{1-p_1p_2e^{-(d-d_0)/\lambda_s}} \quad (1)$$

in which p_1 and p_2 represent the spin polarizations of LSMO and Co electrodes, separately, d is the thickness of the organic layer, d_0 denotes the "ill-defined" layer formed during the Co deposition process, and λ_s is the spin diffusion length [32, 46]. This equation was utilized to fit the MR value in Figure 6b,c to achieve the three vital spin-related parameters, p_1p_2, d_0, and λ_s. As illustrated in Figure 6a, the fitted parameters: $p_1p_2 = 0.2183$, $d_0 = 10$ nm, and $\lambda_s = 66.9$ nm, were in good agreement with the MR data for DPP-BTCN-C1 at 10 K. Additionally, the spin-related parameters derived from the MR data of another polymer were as follows: $p_1p_2 = 0.2068$, $d_0 = 10$ nm, and $\lambda_s = 66.5$ nm. The reduced interfacial spin polarization injection efficiency, generally attributed to the conductivity mismatch between the FM electrode and the polymer layer, is the primary factor responsible for the lower-than-expected value of p_1p_2. A 10 nm thick "ill-defined" layer within the polymer interlayer indicated the presence of an interfacial reaction and the penetration of the Co electrode during the thermal deposition of the metal electrode. According to the research based on polymer P(NDI2OD-T2) [32], where an AlOx buffer layer is used to suppress the penetration behavior of metal atoms, the spin diffusion length does not change significantly, indicating that the spin diffusion length mainly depends on the intrinsic properties of the polymer

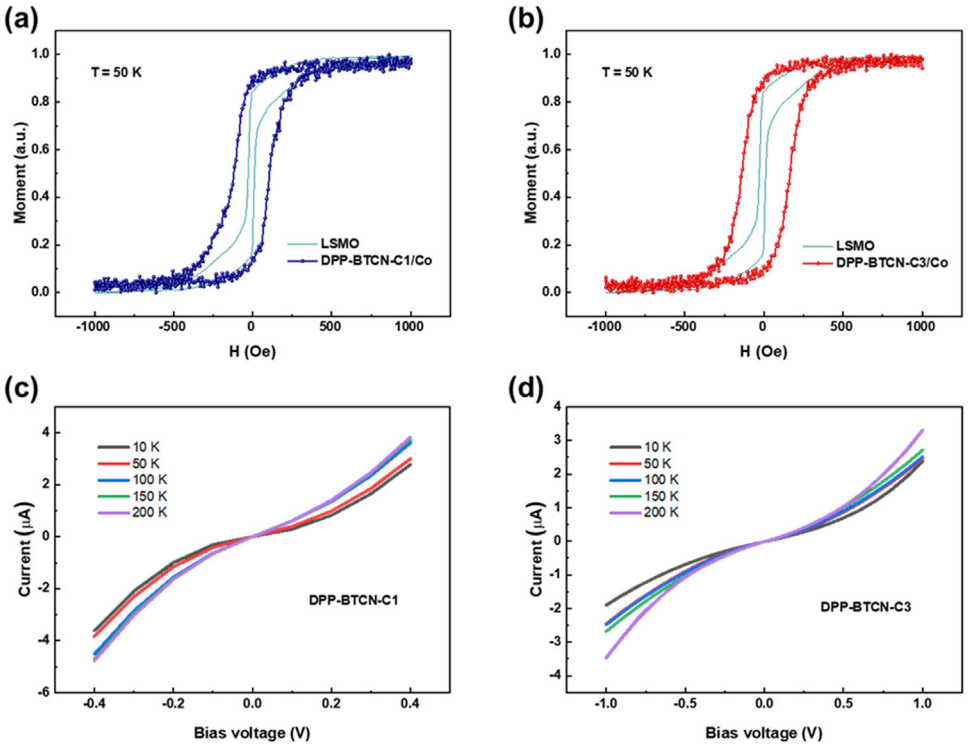

FIGURE 5 | (a,b) The hysteresis loops of (a) DPP-BTCN-C1/Co and (b) DPP-BTCN-C3/Co. (c,d) The *I–V* characteristic curves of the OSVs devices with (c) DPP-BTCN-C1 and d) DPP-BTCN-C3 as active layers.

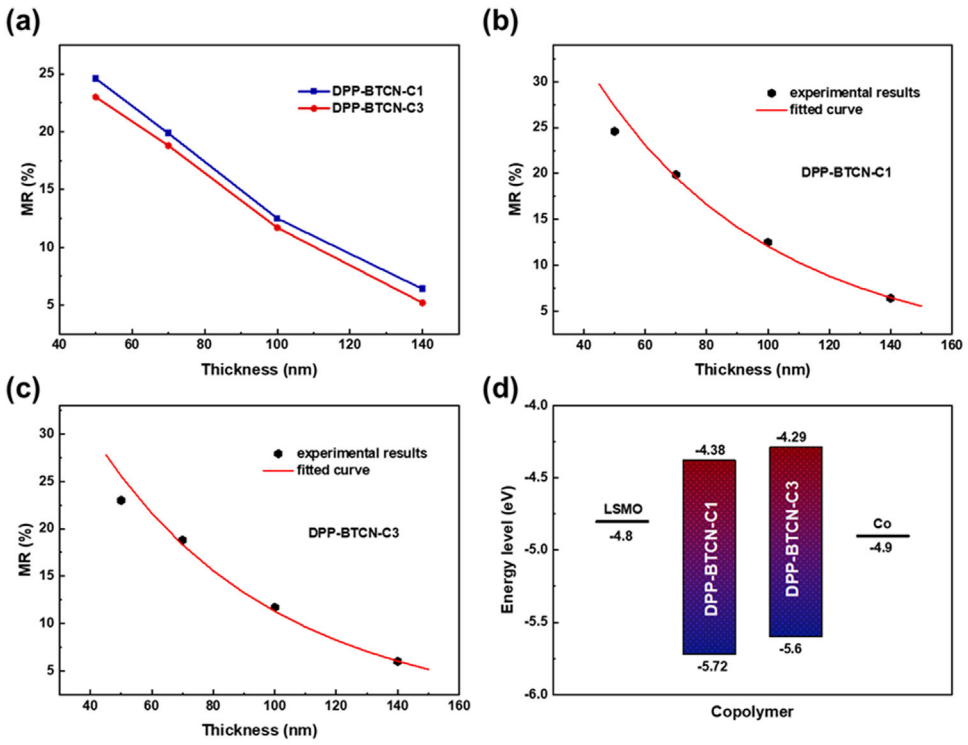

FIGURE 6 | (a) Comparison of MR values of OSVs devices with different film thicknesses of the two polymers at 10 K. (b,c) MR ratios of the OSVs as a function of the thickness of (b) DPP-BTCN-CI and (c) DPP-BTCN-C3 thin films. (d) The energy diagram of the polymeric OSVs devices.

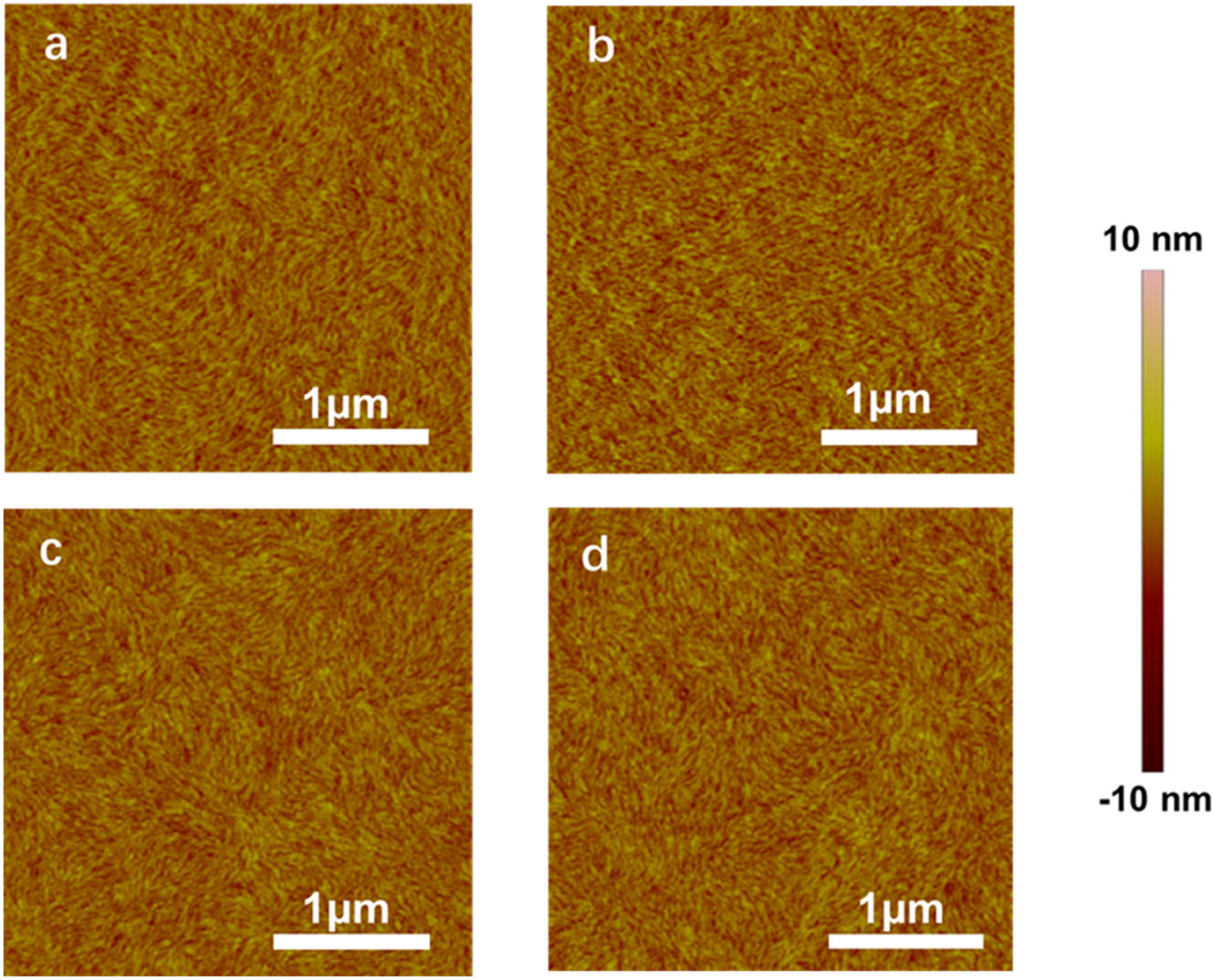

FIGURE 7 | AFM images of polymer films. (a) as-cast DPP-BTCN-C1 thin film, (b) annealed DPP-BTCN-C1 thin film, (c) as-cast DPP-BTCN-C3 thin film, (d) annealed DPP-BTCN-C3 thin film.

itself. The relatively thinner hybrid interfacial layer between FM electrodes and polymers was due to the slow Co thermal evaporation rate (0.1 Å/s) employed during the device fabrication process. Besides, long spin diffusion lengths of about 66 nm were obtained for both polymers, which demonstrated that this type of DPP-based D–A copolymers had excellent spin transport properties. The values of λ_s were acquired by fitting the experimental MR values obtained from devices with varying polymer thicknesses using Equation (1). Notably, the spin polarization injection efficiency between the two polymers showed a relatively obvious difference. From these observations, we inferred that the injection efficiency of the spin-polarized carriers was influenced by the injection barrier between the molecular orbital energy levels of the polymers and the work function of the metal electrodes. The work function of the FM electrodes applied in our OSVs devices was commonly −4.9 eV for Co and −4.8 eV for LSMO. The energy level structures of the polymers were characterized by the aforementioned UPS measurements and the optical bandgap. The energy level diagrams for the LSMO/D–A polymer/Co stacking architecture of the two OSVs were showcased in Figure 6d. Based on the results of the preceding charge carrier transport studies, it was evident that the electron transport predominated in both polymers. Consequently, we proposed that in the OSVs devices, the spin transport mechanism was also likely dominated by spin-polarized electron injection and transport. The electron injection barrier between the work function of the Co electrode and the LUMO energy level of DPP-BTCN-C1 was approximately 0.52 eV, which was lower than that between the work function of the Co electrode and the LUMO energy level of DPP-BTCN-C3 (0.61 eV). Therefore, the enhanced spin polarization of DPP-BTCN-C1 may originate from the better alignment of its energy level in the device structures [35, 38]. In the design of DPP-based D–A polymers for the preparation of OSVs devices, the selection of materials with suitable energy levels was critical to optimizing device performance.

The analyses of the film morphologies and microstructure were performed to further reveal the structure-performance relationships in both PFETs and OSVs. To study the effect of the distance between the branch points of the alkyl side chain and the conjugated main chains on the surface morphology of the polymer films, we employed atomic force microscopy

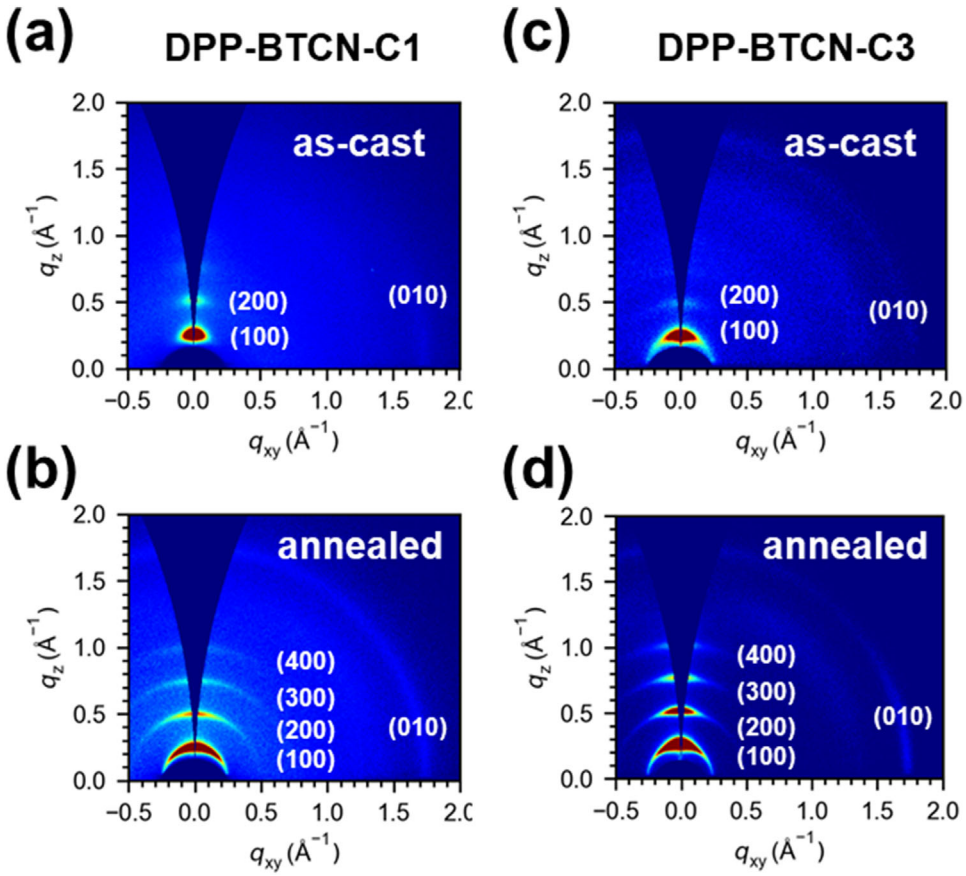

FIGURE 8 | 2D GIWAX images of polymer films. (a) as-cast DPP-BTCN-C1 thin film, (b) annealed DPP-BTCN-C1 thin film, (c) as-cast DPP-BTCN-C3 thin film, (d) annealed DPP-BTCN-C3 thin film.

(AFM) in the trapping mode. For the TGBC-configure PFETs, the root-mean-square (RMS) roughness of the as-cast thin film for DPP-BTCN-C1 and DPP-BTCN-C3 was 1.00 and 0.73 nm, respectively, and increased to 1.19 and 0.86 nm for the annealed film. As for the OSVs devices based on the LSMO substrate, the as-cast films exhibited an RMS surface roughness value of 0.84 and 0.81 nm for DPP-BTCN-C1 and DPP-BTCN-C3, respectively. After annealing, the roughness values increased to 0.94 and 0.86 nm (Figure 7), respectively. These low roughness and homogeneous surfaces provided essential conditions for the successful fabrication of the electrical and spintronic devices. Moreover, we measured TEM imaging with element mapping to examine the cross-sections of the OSVs based on DPP-BTCN-C1. The elements distribution revealed that both the LSMO/DPP-BTCN-C1 and DPP-BTCN-C1/Co interfaces were greatly clear (Figure S8). In addition, to get the microstructural information of the two polymers on the LSMO substrate, the 2D grazing-incidence wide-angle X-ray scattering (2D-GIWAXS) technique was conducted. In comparison to the as-cast thin films, the annealed polymeric films exhibited an enhanced solid-state crystallinity and more ordered packing due to the reinforced (h00) diffraction peaks (Figure 8). The GIWAXS pattern of the two polymers represented more distinct (010) peaks in the in-plane directions, which indicated these DPP-based polymers adopted an edge-on dominated packing mode [47]. Based on the out-of-plane and in-plane diffraction peaks, we obtained the d-d and π–π distances for the polymer thin films via the formula of $d = 2\pi/q$. From the calculated results, the values of the π–π distances were similar for DPP-BTCN-C1 (3.62 Å) and DPP-BTCN-C3 (3.63 Å) thin films. In addition, the distance values of the d-spacing were calculated to be 24.46 and 24.78 Å for DPP-BTCN-C1 and DPP-BTCN-C3, respectively. From the results of the measurements, it can be inferred that the varying branch points induced similar π–π distances and distinct d-d distances in the D–A polymers. The proximity of the branch points to the conjugated backbone resulted in shorter d-d distances. Consequently, the corresponding OSVs devices exhibited higher MR values, which were considered advantageous for the fabrication of spintronic devices. This finding unequivocally demonstrated that the diversity of alkyl chains played a significant role in the microstructures of the D–A polymer films, and then modulated the charge/spin transport properties.

3 | Conclusions

Two D–A conjugated polymers based on DPP units with different side-chain branching points have been synthesized, and the effect of their chemical structures on both charge and spin transport properties has been systematically investigated. In the context of OFETs and OSVs devices, both copolymers exhibited excellent charge and spin-polarized carrier transport properties. OFETs devices based on DPP-BTCN-C1 achieved an electron mobility of 0.36 cm^2 V^{-1} s^{-1}, and the OSVs exhibited a MR value of up to 24.6 % at 10 K. The performance metrics of both devices were slightly superior to those of their counterparts based on DPP-BTCN-C3.

Through the analysis of the energy level structure, it was observed that polymers with branch points closer to the conjugated backbones exhibited a lower barrier gap between their LUMO energy level and the work function of the Co electrode, which facilitated a more efficient electron injection. To further extract spin-related parameters, we conducted a fitting analysis of the MR effect as a function of polymer thickness. At 10 K, the maximum spin diffusion length of the two polymers reached about 66.9 nm. Additionally, the spintronic devices based on DPP-BTCN-C1 demonstrated a higher spin polarization efficiency, which contributed to the elevated MR values in their corresponding devices. The characterization of the microstructures further revealed that the d-d distance in DPP-BTCN-C1 is relatively shorter, consistent with our group's previous findings, which is speculated to be one of the contributing factors to the superior performance of its OSVs devices. Further investigation into the correlation between the extensive structural tunability of D–A polymers and device performance will provide a foundation for the design of high-performance transport materials and functional spintronic devices.

4 | Experimental Section

4.1 | Device Fabrication

The PFETs were prepared on Corning glass with a TGBC configuration. The gold source-drain electrodes were patterned via a shadow mask with a channel width of 5500 μm and a channel length of 55 μm, respectively. Then, the polymer solution (~5 mg mL^{-1} in $CHCl_3$) was spin-coated on the substrate with pre-prepared source and drain electrodes in the nitrogen glovebox and annealed at an appropriate temperature. Subsequently, the solution of poly(methylmethacrylate) (PMMA) was spin-coated on the polymer thin film, which worked as the dielectric layer. The PMMA layer was thermally annealed at 80°C for 30 min to ensure complete curing. Aluminum was then thermally evaporated as the gate electrode on the PMMA layers under vacuum conditions. As for polymeric OSVs devices, first, the LSMO electrode was deposited by a physical pulsed laser deposition method on $SrTiO_3$ substrate and annealed for 60 min in 30 torr oxygen conditions. Then, the LSMO electrodes were patterned into strip shapes via reactive ion etching in an Ar atmosphere. Next, polymeric chloroform solutions were spin-coated on the LSMO electrodes with different solution concentrations and spin coating rates. Subsequently, the polymer films were thermally annealed at 110°C for 10 min to enhance their crystallinity. Finally, the Co electrodes served as the top electrode, which was thermally evaporated with the aid of shadow masks.

4.2 | Magnetic and Magneto-Transport Measurements

The M-H curves of LSMO and Co electrodes were measured using a Quantum Design PPMS and Quantum Design VSM. The magnetic-related transport was measured by PPMS with a closed-cycle helium cryostat in the mode of constant current, and the *I–V* curves were measured by an external Keithley 4200 semiconductor parameter analyzer.

Acknowledgements

The authors are grateful for the financial support from the Key R&D Program of China (2024YFA1209600), the National Natural Science Foundation of China (22021002), the Strategic Priority Research Program of the Chinese Academy of Sciences (XDB30000000), and Beijing National Laboratory for Molecular Sciences (BNLMS-CXXM-202101). The authors thank the beamlines BL02U2 and BL14B1 of Shanghai Synchrotron Radiation Facility for providing the beam time for 2D-GIWAXS measurements, and Dr. Jianyao Huang for his help on 2D-GIWAXS image processing software.

Conflicts of Interest

The authors declare no conflicts of interest.

Data Availability Statement

The data that support the findings of this study are available from the corresponding author upon reasonable request.

References

1. L. Bai, W. Feng, S. Liu, L. Šmejkal, Y. Mokrousov, and Y. Yao, "Altermagnetism: Exploring New Frontiers in Magnetism and Spintronics," *Advanced Functional Materials* 34 (2024): 2409327, https://doi.org/10.1002/adfm.202409327.

2. J. T. Gish, D. Lebedev, T. W. Song, V. K. Sangwan, and M. C. Hersam, "Van der Waals Opto-spintronics," *Nature Electronics* 7 (2024): 336–347, https://doi.org/10.1038/s41928-024-01167-3.

3. J. A. C. Incorvia, T. P. Xiao, N. Zogbi, et al., "Spintronics for Achieving System-Level Energy-Efficient Logic," *Nature Reviews Electrical Engineering* 1 (2024): 700.

4. L. Guo, S. Hu, X. Gu, et al., "Emerging Spintronic Materials and Functionalities," *Advanced Materials* 36 (2024): 2301854.

5. D. Li and G. Yu, "Innovation of Materials, Devices, and Functionalized Interfaces in Organic Spintronics," *Advanced Functional Materials* 31 (2021): 2100550, https://doi.org/10.1002/adfm.202100550.

6. T. D. Nguyen, G. Hukic-Markosian, F. Wang, et al., "Isotope Effect in Spin Response of π-Conjugated Polymer Films and Devices," *Nature Materials* 9 (2010): 345.

7. S. Sanvito and M. Spintronics, "Molecular Spintronics," *Chemical Society Reviews* 40 (2011): 3336–3355, https://doi.org/10.1039/c1cs15047b.

8. J. Devkota, R. Geng, R. C. Subedi, and T. D. Nguyen, "Organic Spin Valves: A Review," *Advanced Functional Materials* 26 (2016): 3881–3898, https://doi.org/10.1002/adfm.201504209.

9. Z. H. Xiong, D. Wu, Z. Valy Vardeny, and J. Shi, "Giant Magnetoresistance In Organic Spin-Valves," *Nature* 427 (2004): 821–824, https://doi.org/10.1038/nature02325.

10. S. Schott, E. R. McNellis, C. B. Nielsen, et al., "Tuning the Effective Spin-Orbit Coupling in Molecular Semiconductors," *Nature Communications* 8 (2017): 15200.

11. D. Li, X. Wang, Z. Lin, et al., "Tuning Charge Carrier and Spin Transport Properties via Structural Modification of Polymer Semiconductors," *ACS Applied Materials & Interfaces* 11 (2019): 30089, https://doi.org/10.1021/acsami.9b07863.

12. X. Song, X. Wang, Y. Li, et al., "2D Semiconducting Metal–Organic Framework Thin Films for Organic Spin Valves," *Angewandte Chemie International Edition* 59 (2020): 1118–1123, https://doi.org/10.1002/anie.201911543.

13. X. Song, C. Jin, H. Chen, et al., "Two-Dimensional Conductive Metal–Organic Framework Reinforced Spinterface in Organic Spin Valves," *CCS Chemistry* 6 (2024): 208–217, https://doi.org/10.31635/ccschem.023.202302859.

14. X. Liu, H. Li, W. Zhang, et al., "Magnetoresistance in Organic Spin Valves Based on Acid-Exfoliated 2D Covalent Organic Frameworks Thin Films," *Angewandte Chemie International Edition* 62 (2023): 202308921, https://doi.org/10.1002/anie.202308921.

15. C. Nicolaides, F. Bazzi, E. Vouros, et al., "Metal-Free Organic Radical Spin Source," *Nano Letters* 23 (2023): 4579.

16. X. Wei, D. Li, X. Liu, et al., "Magnetoresistance Effect of Pyridine-Capped s-Indacene-Based Conjugated Radicals," *Materials Horizons* 12 (2025): 1524.

17. J. Wang, C. Zhang, H. Liu, et al., "Spin-Optoelectronic Devices Based on Hybrid Organic-inorganic Trihalide Perovskites," *Nature Communications* 10 (2019): 129, https://doi.org/10.1038/s41467-018-07952-x.

18. J. Wang, C. Zhang, H. Liu, et al., "Tunable Spin Characteristic Properties in Spin Valve Devices Based on Hybrid Organic–Inorganic Perovskites," *Advanced Materials* 31 (2019): 1904059, https://doi.org/10.1002/adma.201904059.

19. H. Liu, C. Zhang, H. Malissa, et al., "Organic-Based Magnon Spintronics," *Nature Materials* 17 (2018): 308–312, https://doi.org/10.1038/s41563-018-0035-3.

20. S. Liang, Z. Yu, X. Devaux, et al., "Quenching of Spin Polarization Switching in Organic Multiferroic Tunnel Junctions by Ferroelectric "Ailing-Channel" in Organic Barrier," *ACS Applied Materials & Interfaces* 10 (2018): 30614–30622, https://doi.org/10.1021/acsami.8b11437.

21. S. Liang, H. Yang, H. Yang, et al., "Ferroelectric Control of Organic/Ferromagnetic Spinterface," *Advanced Materials* 28 (2016): 10204–10210.

22. W. Zhang, K. Shi, J. Lai, et al., "Record-High Electron Mobility Exceeding 16 cm 2 V −1 s −1 in Bisisoindigo-Based Polymer Semiconductor With a Fully Locked Conjugated Backbone," *Advanced Materials* 35 (2023): 2300145, https://doi.org/10.1002/adma.202300145.

23. S. H. Kumar Paleti, Y. Kim, J. Kimpel, M. Craighero, S. Haraguchi, and C. Müller, "Impact of Doping on the Mechanical Properties of Conjugated Polymers," *Chemical Society Reviews* 53 (2024): 1702–1729, https://doi.org/10.1039/D3CS00833A.

24. K. Shi, W. Zhang, D. Gao, et al., "Well-Balanced Ambipolar Conjugated Polymers Featuring Mild Glass Transition Temperatures Toward High-Performance Flexible Field-Effect Transistors," *Advanced Materials* 30 (2018): 1705286, https://doi.org/10.1002/adma.201705286.

25. X. Wei, Q. Che, W. Zhang, et al., "Bisazathienoisoindigo-Based Conjugated Polymers: Synthesis, Characterization, and the Influence of Inner Bridging Units on the Quinoidal Character and Charge Transport Property," *Macromolecules* 57 (2024): 554.

26. T. Yang, Y. Qin, X. Gu, and X. Sun, "Molecular Design for Enhanced Spin Transport in Molecular Semiconductors," *Nano Research* 16 (2023): 13457.

27. M. Ding, X. Gu, L. Guo, et al., "The Prospects of Organic Semiconductor Single Crystals for Spintronic Applications," *Journal of Materials Chemistry C* 10 (2022): 2507.

28. J. Tsurumi, H. Matsui, T. Kubo, et al., "Coexistence Of Ultra-Long Spin Relaxation Time And Coherent Charge Transport In Organic Single-Crystal Semiconductors," *Nature Physics* 13 (2017): 994.

29. S. Schott, U. Chopra, V. Lemaur, et al., "Polaron Spin Dynamics In High-Mobility Polymeric Semiconductors," *Nature Physics* 15 (2019): 814.

30. A. Nachawaty, T. Chen, F. Ibrahim, et al., "Voltage-Driven Fluorine Motion for Novel Organic Spintronic Memristor," *Advanced Materials* 36 (2024): 2401611, https://doi.org/10.1002/adma.202401611.

31. C. Ye, J. Jiang, S. Zou, W. Mi, and Y. Xiao, "Core–Shell Three-Dimensional Perovskite Nanocrystals With Chiral-Induced Spin Selectivity for Room-Temperature Spin Light-Emitting Diodes," *Journal of the American Chemical Society* 144 (2022): 9707–9714, https://doi.org/10.1021/jacs.2c01214.

32. F. Li, T. Li, F. Chen, and F. Zhang, "Excellent Spin Transport in Spin Valves Based on the Conjugated Polymer With High Carrier Mobility," *Scientific Reports* 5 (2015): 9355, https://doi.org/10.1038/srep09355.

33. Y. C. Zhang, W. F. Zhang, Z. H. Chen, L. P. Wang, and G. Yu, "Recent Developments in Polymer Semiconductors With Excellent Electron Transport Performances," *Chemical Society Reviews* 54 (2025): 2483–2519, https://doi.org/10.1039/D4CS00504J.

34. L. Ding, Z. D. Yu, X. Y. Wang, et al., "Polymer Semiconductors: Synthesis, Processing, and Applications," *Chemical Reviews* 123 (2023): 7421.

35. D. Li, Y. H. Zheng, M. Yang, et al., "Molecular and Interfacial Adjustment of Magnetoresistance in Organic Spin Valves Using Isoindigo-Based Polymers," *ACS Materials Letters* 4 (2022): 1065–1073, https://doi.org/10.1021/acsmaterialslett.2c00322.

36. N. H. Zheng, Z. Z. Lin, Y. H. Zheng, et al., "Room-Temperature Stable Organic Spin Valves using Solution-processed Ambipolar Naphthalenediimide-based Conjugated Polymers," *Organic Electronics* 81 (2020): 105684, https://doi.org/10.1016/j.orgel.2020.105684.

37. Y. H. Zheng, Y. Feng, D. Gao, et al., "Magnetoresistance and Spinterface of Organic Spin Valves Based on Diketopyrrolopyrrole Polymers," *Advanced Electronic Materials* 5 (2019): 1900318, https://doi.org/10.1002/aelm.201900318.

38. X. Yang, A. Guo, J. Yang, et al., "Halogenated-Edge Polymeric Semiconductor For Efficient Spin Transport," *Nature Communications* 15 (2024): 8368.

39. Y. Zhao, Z. Li, D. Wang, et al., "High Performance and Colorful Polymer Thermoelectrics With Imprinted Porous Film," *Advanced Materials* 36 (2024): 2407692, https://doi.org/10.1002/adma.202407692.

40. M. Li, W. Li, J. Zhou, et al., "N -oxide-Functionalized Bipyridines as Strong Electron-Deficient Units to Construct High-Performance n-Type Conjugated Polymers," *Advanced Science* 12 (2025): 2414059, https://doi.org/10.1002/advs.202414059.

41. Z. H. Chen, D. Gao, J. Y. Huang, Z. P. Mao, W. F. Zhang, and G. Yu, "Thiazole-Flanked Diketopyrrolopyrrole Polymeric Semiconductors for Ambipolar Field-Effect Transistors With Balanced Carrier Mobilities," *ACS Applied Materials & Interfaces* 8 (2016): 34725, https://doi.org/10.1021/acsami.6b08543.

42. Y. K. Zhou, Q. Che, W. F. Zhang, et al., "Isoquinoline-1,3-dione-derived Conjugated Polymers for Field-effect Transistors: Synthesis, Properties, and the Effect of Inner Aromatic Bridges," *Polymer Chemistry* 14 (2023): 2333–2343, https://doi.org/10.1039/D3PY00063J.

43. S.-J. Wang, D. Venkateshvaran, M. R. Mahani, et al., "Long Spin Diffusion Lengths in Doped Conjugated Polymers Due to Enhanced Exchange Coupling," *Nature Electronics* 2 (2019): 98.

44. R. Steyrleuthner, R. Di Pietro, B. A. Collins, et al., "The Role of Regioregularity, Crystallinity, and Chain Orientation on Electron Transport in a High-Mobility n-Type Copolymer," *Journal of the American Chemical Society* 136 (2014): 4245–4256, https://doi.org/10.1021/ja4118736.

45. T. Yang, Y. Qin, M. Wu, et al., "Spin-Lifetime Probe for Detecting Intramolecular Noncovalent Interaction in Organic Semiconductors," *Advanced Materials* 36 (2024): 2410695, https://doi.org/10.1002/adma.202410695.

46. T. Yang, Y. Qin, M. Wu, et al., "Structural Isomeric Effect on Spin Transport in Molecular Semiconductors," *Advanced Materials* 36 (2024): 2402001.

47. Y. C. Pan, J. Y. Huang, D. Gao, Z. H. Chen, W. F. Zhang, and G. Yu, "An Insight Into the Role of Side Chains in the Microstructure and Carrier Mobility of High-performance Conjugated Polymers," *Polymer Chemistry* 12 (2021): 2471.

Supporting Information

Additional supporting information can be found online in the Supporting Information section.

Supporting File: adma72403-sup-0001-SuppMat.docx.